THE JOHN JAEGER MEMORIAL AWARD PAPER 2023

GEOTECHNICAL VARIABILITY: IN THE GROUND AND THROUGHOUT A CAREER

Mark Jaksa
University of Adelaide, Australia

https://doi.org/10.56295/AGJ5841

ABSTRACT

This paper presents three aspects of geotechnical engineering research that have been conducted throughout the author's career and concludes with a brief treatment of the use of physical models in teaching. The first research topic deals with quantifying the large-scale spatial variability of the Keswick Clay in Adelaide by means of undrained shear strength data acquired from several private consulting companies and government departments, incorporating a large number of site investigations. The mathematical technique of geostatistics is used, and it is observed that kriging with a spherical model, with a range of influence of 1000 m, a nugget of 1500 kPa^2, and a sill of 2500 kPa^2, is able to generate good estimates of the undrained shear strength of the Keswick Clay that can be used for preliminary design purposes. Secondly, the ground improvement technique of rolling dynamic compaction (RDC) is examined in the field and in the laboratory, and numerically by means of artificial neural networks (ANNs). It is observed that RDC is able to improve the ground to depths in excess of 3 m, and the use of transparent soils in the laboratory provides useful insights regarding the influence of RDC on the subsurface profile. In addition, ANNs facilitate the development of reliable models for the prediction of the level of ground improvement due to RDC. The third and final research topic presented involves ground improvement on the Moon. It is a work-in-progress, and early results are presented in this fascinating and exciting endeavour. The paper concludes with a brief treatment of the use of three different physical models used in teaching. It is observed that incorporating demonstrations involving physical models in teaching is helpful for enhancing student learning and engagement.

1 INTRODUCTION

I am deeply honoured and immensely humbled to have been selected by the Australian Geomechanics Society (AGS) to be the 2023 recipient of the *John Jaeger Memorial Award*. I am very proud to have been a member of the AGS since I graduated in civil engineering from the University of Adelaide in 1984. Over the span of a career, the AGS has been family to me, and I have made many wonderful, lifelong friendships with fellow members. It has been an enormous privilege and honour to serve, and belong to, the AGS.

If you'll indulge me a little, the title of this paper is a play on words on the theme of variability, and sort of sums up my career in many ways. My research journey began in 1988 when, after having spent four years in industry, I was employed as a Tutor (Lecturer Level A, in the present-day parlance) in the Department of Civil Engineering at the University of Adelaide, and at the same time, I enrolled in a part-time PhD. My thesis, which was submitted for examination in 1995, was entitled "The influence of spatial variability on the geotechnical design properties of a stiff, overconsolidated clay" and focusses on characterising the spatial variability of clay (Jaksa 1995). Since then, as curiosity and opportunities often do, my research career has also been one of diversity. I have studied and enjoyed many different aspects of geotechnical engineering, by exploring the following topics: spatial variability of soils; geostatistics; probabilistic analysis and design; optimisation of site investigations; machine learning; ground improvement using rolling dynamic compaction, dynamic compaction and electro-osmosis; expansive and unsaturated soils; residential foundation design; slope stability and riverbank collapse modelling; numerical modelling; earthquake geotechnical engineering; environmental geotechnics and landfills; in situ testing of soils; tensile capacity of small ground anchors; geotechnical engineering education; and lunar geotechnics. Hence, one could say that my career has been one immersed in variability.

Clearly, there is not enough space to cover each of these topics, nor would it make much sense, as this work is covered elsewhere in the literature. Instead, I'd like to pay homage to the theme of variability by, in terms of my research journey, first looking at the past, where I began with spatial variability, then examining more recent research endeavours by exploring ground improvement, and subsequently peering into the future and exploring the futuristic topic of lunar geotechnics. In the final part of this paper, I'd like to touch on the use of demonstration models in teaching. I hope that you, like me, find these topics fascinating and engaging.

2 BEGINNINGS: SPATIAL VARIABILITY

As mentioned above, my PhD thesis examined the spatial variability of a clay, in fact, the Keswick Clay, which is an extremely reactive, overconsolidated clay that underlies much of the Adelaide city and metropolitan areas (Jaksa 1995). It is remarkably similar in geotechnical characteristics to the ubiquitous London Clay (Cox 1970). In my thesis, I tested and analysed the small-scale variation in shear strength of the clay by means of 224 cone penetration tests (CPTs) performed in a 50 m × 50 m area, as well as a single CPT pushed horizontally into an embankment consisting of Keswick Clay. This work is summarised by Jaksa et al. (2000). However, in my thesis, I also examined the large-scale variability of the shear strength of the Keswick Clay using geostatistics, and it is this aspect of spatial variability that I would like to present in this paper.

To characterise the 3D spatial variability over relatively large distances, a database known as *KESWICK* was compiled from 10,140 test records from 380 boreholes, which involved a wide range of geotechnical test types. The data were obtained from records kindly provided by seven geotechnical engineering consultants in Adelaide and one South Australian Government department. The test method with the largest amount of shear strength data relating to the Keswick Clay was undrained shear strength, s_u, data obtained from unconsolidated undrained (UU) triaxial tests. Whilst this test method is sub-optimal, it was the only single test method within *KESWICK* which provided sufficient data to facilitate large-scale, spatial variability analyses. Figure 1 shows a plan view of the 143 spatial locations of the Keswick Clay s_u data included in the *KESWICK* database, between depths of 0 to 3 m below the ground surface. Additional data are available at greater depths, but these are not included in the analyses that follow.

The spatial variability analyses that follow are those based on the now universal branch of statistics known as geostatistics that deals with the spatiotemporal variation of natural phenomena (Journel & Huijbregts 1978). At the heart of geostatistics is the semivariogram, which expresses the degree of spatial dependence between samples along a specific orientation and represents the degree of continuity of the property in question. The semivariogram, γ_h, is defined by the following relationship:

$$\gamma_h = \frac{1}{2}\mathrm{E}[(X_{i+h} - X_i)^2] \tag{1}$$

where: X_i is the value of the property (or regionalised variable) X, at location, i; X_{i+h} is the value of the property, X, at location, $i+h$; h is the displacement between the data pairs; and E[…] is the expected value.

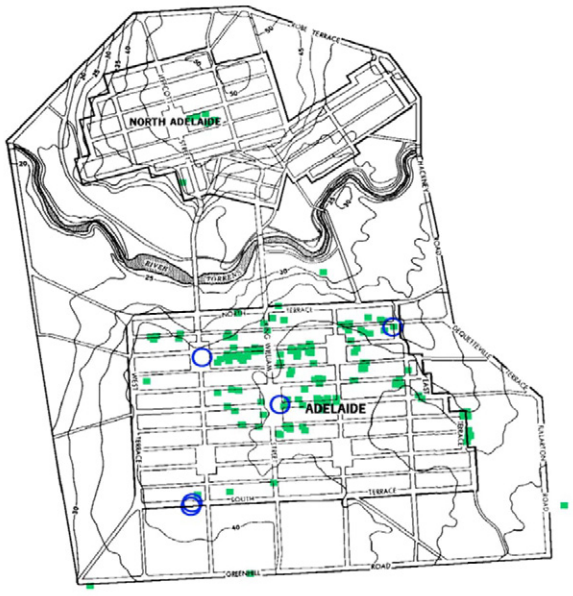

Figure 1: Spatial distribution of s_u data included in the *KESWICK* database in the Adelaide city area. The green squares indicate the locations of the 143 data used in the spatial variability analyses, whereas the blue circles indicate the locations of additional, subsequently available data, which are discussed later. (After Jaksa 1995.)

However, in the ground, it is not possible to know γ_h at all locations; rather it is approximated from measured data. Hence, the experimental semivariogram, γ_h^*, is determined from the following equation:

$$\gamma_h^* = \frac{1}{2N}\sum_{i=1}^{N}(X_{i+h} - X_i)^2 \quad (2)$$

where: N is the total number of data points.

Substituting the 143 s_u measurements into Equation (2) yields the experimental semivariogram shown in Figure 2. Superimposed on Figure 2 is a spherical model [Equation (3)] that is often adopted in geostatistics to generate a continuous, best-fit function to the experimental semivariogram.

$$\begin{aligned} \gamma_h &= C\left(\frac{3h}{2a} - \frac{h^3}{2a^3}\right) + C_0 \qquad \text{when } h \le a \\ \gamma_h &= C + C_0 \qquad \text{when } h \ge a \end{aligned} \quad (3)$$

where, also as shown in Figure 2:

- C_0 is defined as the *nugget effect* and arises from the regionalised variable being so erratic over a short distance that the semivariogram rises from zero to the level of the nugget in a distance less than the sampling interval. The nugget effect is the result of three separate phenomena: (i) microstructures within the geological material; (ii) sampling, or statistical, errors; and (iii) measurement errors;
-
- $C + C_0$ is known as the *sill*, which measures half the maximum, on average, squared difference between data pairs; and
- a is defined as the *range of influence*, or simply *range*, and is the distance at which samples become independent of one another. Data pairs separated by distances up to a are correlated, but not beyond.

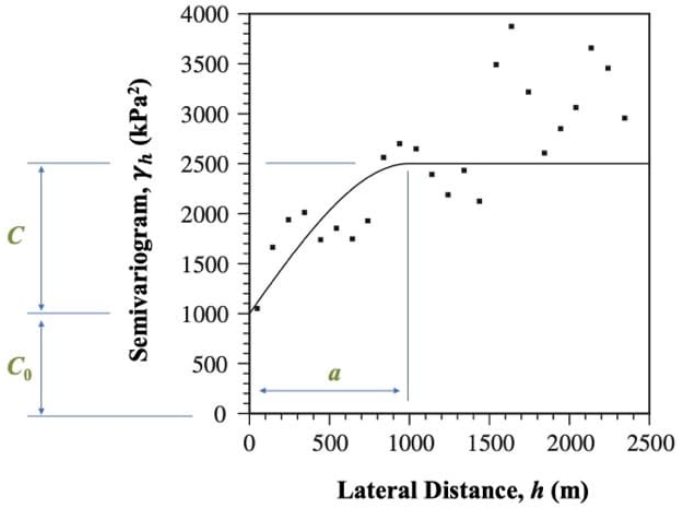

Figure 2: Experimental semivariogram and spherical model of s_u *KESWICK* data. (After Jaksa 1995.)

As can be seen from Figure 2, the spherical model represents the data reasonably well, although less so for lateral distances greater than 1500 m. Figure 3 shows the number of pairs associated with each semivariogram value. As can be seen, for distances greater than 1500 m, the number of pairs contributing to each semivariogram value is much lower, and hence the reliability of the experimental variogram values diminishes.

The spherical model shown in Figure 2, and expressed by Equation (3) above, is associated with the following parameters: a = 1000 m; C_0 = 1500 kPa^2; and C = 1000 kPa^2.

The strength of geostatistics is its ability to predict, with a reasonable degree of accuracy, values at unsampled locations. This process is known as *kriging* (Journel & Huijbregts 1978). In an effort to test the veracity of the derived spatial model, kriging was performed, using the *GEO-EAS* geostatistical software (Englund & Sparks 1991), at the locations shown by blue circles in Figure 1. These represent five new data points that were obtained after the semivariograms, shown in Figure 2, were derived. The results of the kriging at these locations are summarised in Table 1.

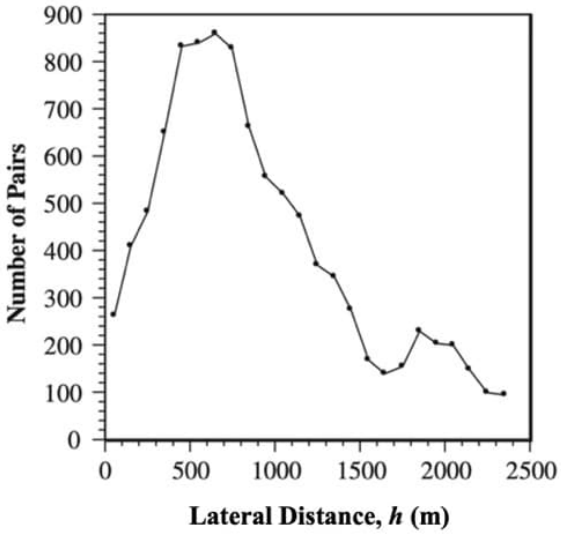

Figure 3: Number of pairs associated with experimental semivariogram in Fig. 2. (After Jaksa 1995.)

Table 1: Comparison between measured and predicted (kriged) s_u values.

Sample No.	Measured (kPa)	Kriged (kPa)	% Error
1	250	217	13.2
2	92	83.4	9.6
3	105	104.4	0.6
4	139	116	16.5
5	111	115	3.6

As can be seen, the geostatistical model performs quite well and demonstrates that spatial variability modelling has the potential to provide useful predictions of s_u at unsampled locations. It should be noted that I do not advocate using kriging in lieu of traditional site investigations involving laboratory and/or in situ testing. On the other hand, spatial variability modelling is a useful additional tool that can provide estimates for initial planning and design.

Due to space constraints, this treatment of the large-scale variability of the shear strength of the Keswick Clay has been necessarily brief. A more detailed account is provided by Jaksa (1995, 2006).

3 RECENT: GROUND IMPROVEMENT

Turning our attention to more recent research endeavours, since 2007, I and several of my former postgraduate students, have enjoyed a fruitful and enjoyable working relationship with ground improvement supplier, manufacturer and contractor Broons. In this section, I'd like to share some of the interesting research that has been undertaken in the field of rolling dynamic compaction.

Rolling dynamic compaction (RDC) involves towing a 3-, 4- or 5-sided module behind a tractor. As the module rotates about its corners, it drops to the ground, thereby imparting a combination of kinetic and potential energy to the ground, which in turn compacts the ground. Since its inception in the late 1940s in South Africa, the technology has evolved, improved and become more mainstream. The research undertaken at the University of Adelaide has focussed on the Broons 4-sided 'impact roller' (Fig. 4a), and the discussion that follows presents the results of some of this work. Collaborative research with Prof. David Airey and his students from the University of Sydney, has examined the 3-sided roller (Fig. 4b) (Li et al. 2022). The benefits of RDC over traditional methods of compaction include its: (i) greater effective depth of compaction; (ii) faster operational speed (9–12 km/h *cf.* 4 km/h for traditional circular drum rollers); and (iii) ability to compact thicker lifts.

In the sub-sections that follow, three examples will be presented of research studies undertaken to understand better the nature of RDC; namely, field and laboratory experimentation, and machine learning.

(a) (b)

Figure 4: Rolling dynamic compaction modules: (a) 4-sided (Broons); and (b) 3-sided (Landpac).

3.1 FIELD EXPERIMENTATION

In his PhD, Dr. Brendan Scott carried out extensive monitoring of the 4-sided module in the field (Scott & Jaksa 2015, Scott et al. 2019, 2020, 2021). A field trial was undertaken at the Iron Duke Mine on the Eyre Peninsula in South Australia using the 8-tonne Broons BH-1300 impact roller. As shown in Figure 5, a 4.19 m thick test pad was constructed in three separate layers (i.e. lifts) of differing thicknesses of loose mine tailings. Figure 5 also shows the locations of four Geokon Model 3500 (230 mm diameter, 6 mm thick) earth pressure cells (EPCs) that were buried within each of the layers.

Pressure measurements from the EPCs were recorded using a bespoke data acquisition system, which obtained measurements at a sampling frequency of 2 kHz (i.e. one sample every 0.0005 seconds). A typical result is presented in Figure 6, where the measurements of Layer 1 are shown. In this case, as the test pad was progressively raised, only the first lift was compacted by RDC; with EPCs 1 and 2 located 670 and 870 mm below the ground surface, respectively.

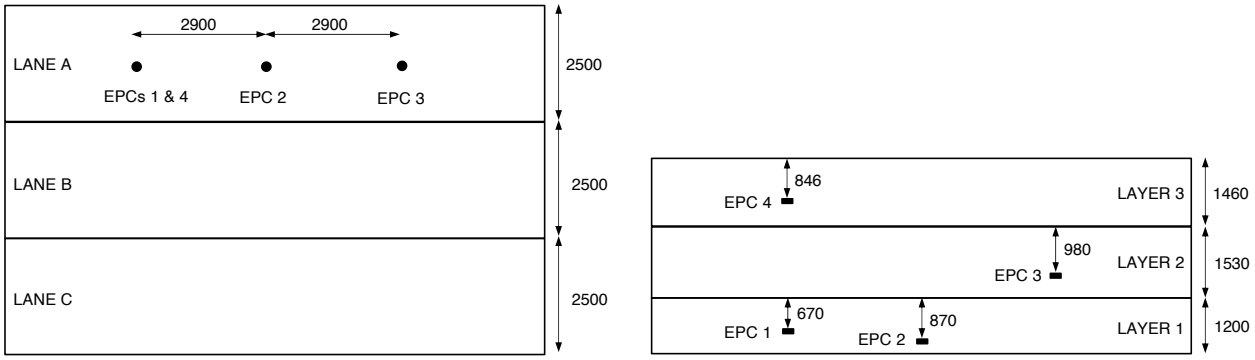

(a) (b)

Figure 5: Test pad layout: (a) plan view, and (b) cross-sectional elevation. Dimensions in mm. (After Scott et al. 2021.)

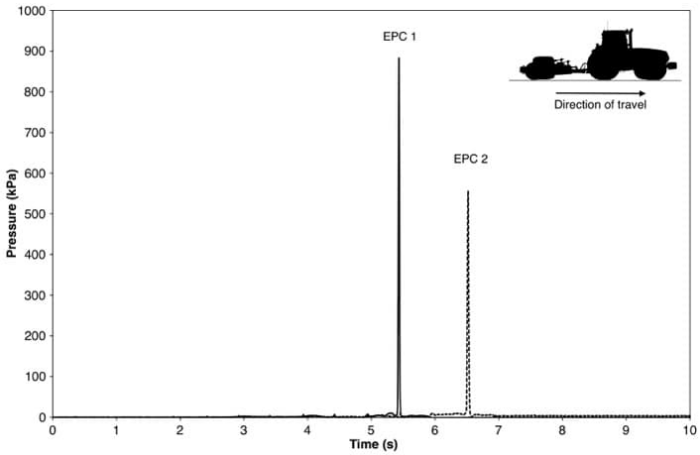

Figure 6: Example results of pressure versus time for a single pass of the impact roller: Layer 1 containing EPCs 1 and 2. (Adapted from Scott et al. 2021.)

As expected, and as can be seen from Figure 6, EPC 1 records a higher pressure than EPC 2, because the former is closer to the ground surface than the latter. It can also be observed that the pressure spike occurs over a very short time period; in fact, 0.05 seconds as presented by Scott et al. (2020).

The results of the four EPCs are summarised in Figure 7, which presents the relationship between measured pressure and depth below the ground surface, with a power curve fitted to the data. As can be seen, pressures reduce exponentially with depth, pressures greater than 100 kPa were recorded 2.0 m below the ground, and the deepest EPC (EPC 2 at 3.85 m depth) recorded a positive pressure.

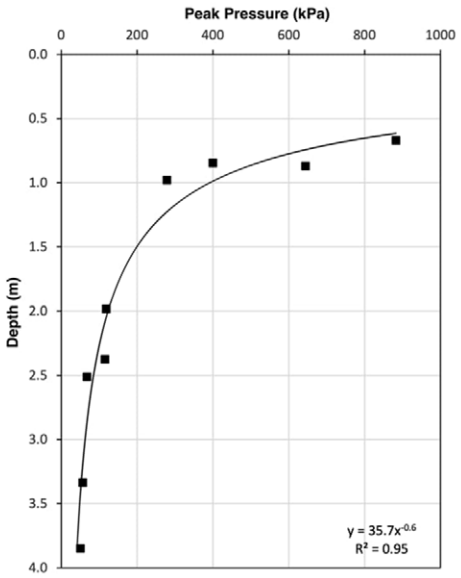

Figure 7: Measured peak pressure against depth with associated best-fit trend line. (Adapted from Scott et al. 2021.)

Augmenting the pressures recorded by the EPCs with dynamic cone penetration, geophysical, and sand-replacement density testing, Scott et al. (2019) was able to demonstrate, for the Iron Duke trial pad, that the effective depth of ground improvement (EDI) (defined as the maximum depth to which significant improvement occurs) was be equal to 2 m.

3.2 LABORATORY EXPERIMENTATION

To understand better the nature of RDC, and to quantify its efficacy across a range of soil types, variables and field conditions, a bespoke testing facility was developed jointly by the University of Adelaide and Broons, as shown in Figure 8. The test rig consists of an elliptical track and two 1.2 m high × 0.75 m wide × 1.075 m long steel bins, which contain the soil to be improved by the RDC model and incorporate buried instrument-ation. A mechanically equivalent, scale model (Fig. 9) is towed along the track by a chain-driven carriage, which is powered by a variable-speed, electric motor. Two physical models of the 4-sided RDC module have been investigated to date using the testing facility. Both models have identical dimensions (115 × 115 × 100 mm) and weigh 3.64 and 5.46 kg and are, respectively, 1:13 scaled replicas of the Broons 4-sided BH-1300 (8-tonne) and BH-1300 HD (12-tonne) 'impact rollers'.

Figure 8: University of Adelaide–Broons RDC laboratory test rig.

Figure 9: Scale model (1:13) replica of Broons BH-1300 4-sided impact roller.

3.2.1 Instrumentation

In order to quantify the efficacy of RDC, several sensors and devices have been developed and/or acquired for this purpose. These include: (i) miniature, 19 mm diameter EPCs, which are fitted with bespoke 3-axis accelerometers (Fig. 10a); (ii) a Tekscan tactile pressure sensor (Fig. 10b); (iii) a high-fidelity 3D scanner (Fig. 10c); and (iv) a nuclear density meter (Fig. 10d). Due to space limitations, only the results obtained from the 3D scanner will be examined in §3.2.2 below.

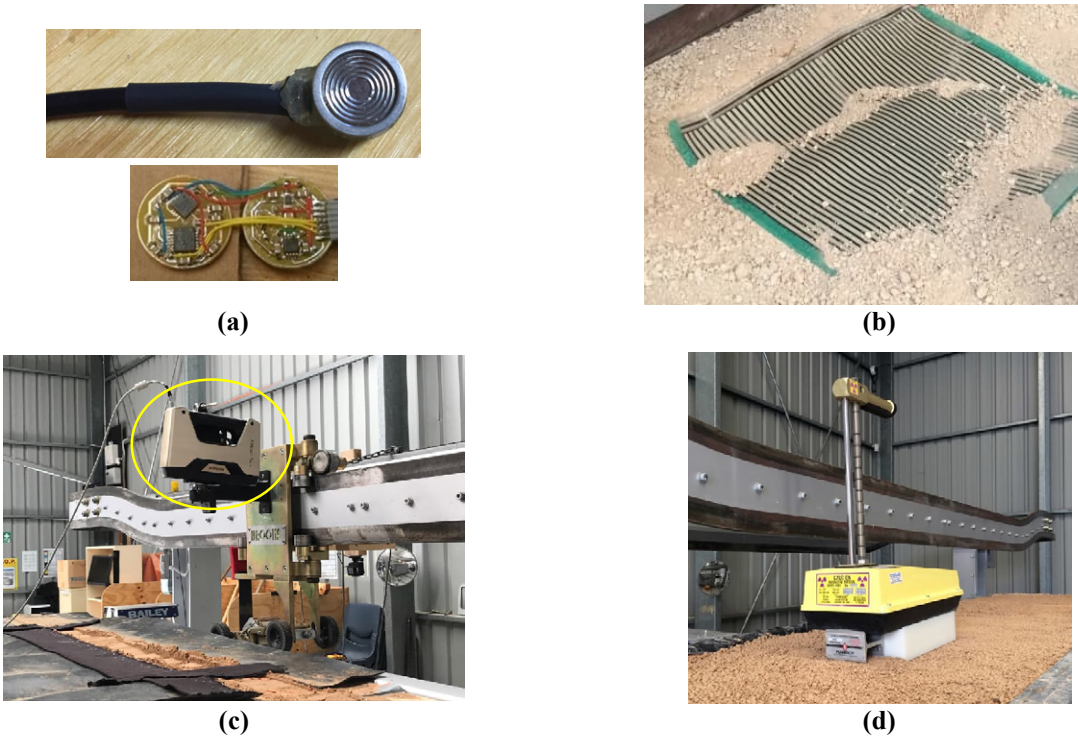

(a) **(b)** **(c)** **(d)**

Figure 10: Laboratory instrumentation: (a) miniature EPC, (b) Tekscan tactile pressure sensor, (c) 3D scanner, and (d) nuclear density meter.

Whilst much work has been performed using the test rig, in a variety of soil types, some of which has been published (Chung et al. 2017, Jaksa et al. 2019), I'd like to focus on some innovative laboratory testing undertaken by my former PhD student Dr. Yue Chen, using transparent soils.

3.2.2 Transparent soils

To obtain deeper insights into the nature of RDC ground improvement, transparent soils were adopted, where particles of high purity fused quartz were used (Fig. 11a). Considering the transparency of the particles and the size of the chamber, which is detailed below, in this study the fused quartz size range is selected to be between 3 and 5 mm, with a mean particle size D_{50} of 3.84 mm. Without the addition of a pore fluid, the assemblage of fused quartz particles is opaque (Fig. 11b). However, when a pore fluid is added to the particles, whose refractive index (RI) matches that of the fused quartz, the 'soil' becomes transparent (Fig. 11c). The pore fluid used in this case is a solution of sodium-thiosulfate treated sodium-iodide (STSI) and the RIs are matched at a temperature of 22°C. The sheet of paper that is visible in Figs. 11b and 11c, is inserted into the assemblage of fused quartz particles, which is 140 mm thick.

(a) **(b)** **(c)**

Figure 11: Transparent soil: (a) fused quartz particles; (b) particles without STSI pore fluid; and (c) particles with STSI pore fluid. (Adapted from Chen et al. 2022.)

The experimental setup, shown previously in Figure 8, was modified to facilitate the testing of transparent soil, as shown in Figure 12. The central acrylic chamber measures 300 mm long × 280 mm wide × 250 mm high.

The objective of this setup was to use particle image velocimetry (PIV) to trace the movement of the particles of a central plane, as the RDC module traversed over the surface of the transparent soil. This plane coincided with the centreline of the RDC module. A speckled pattern was achieved by manually placing numerous particles, which had previously been spray painted black. Preliminary analysis indicated that an optimal speckled pattern was achieved with a density of 1.5×10^{-3} g/mm^2 (or 112.5 g) of black particles.

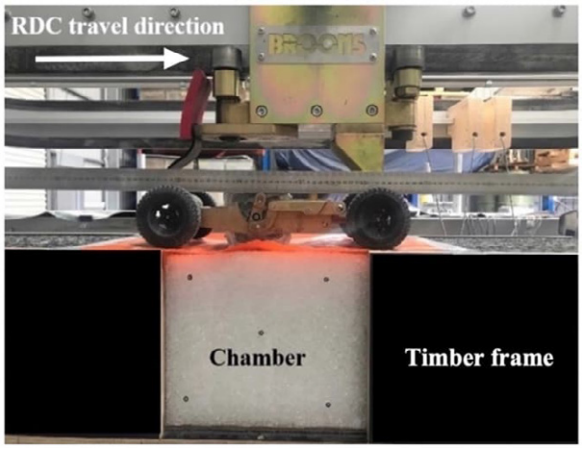

Figure 12: Transparent soil experimental setup. (Adapted from Chen et al. 2022.)

The transparent soil in the chamber was prepared as follows:

1. A temporary panel was placed on the top of the chamber and the front panel was removed.
2. The chamber was tipped on its back and the STSI solution poured into it.
3. The fused quartz particles were then carefully pluviated in successive 50 mm thick layers, to achieve consistent density and to minimise the formation of air bubbles, until the chamber was half-full (i.e. 140 mm).
4. The surface of the transparent soil was then carefully levelled.
5. The black particles were then manually placed on the transparent soil surface to provide an evenly distributed speckled pattern (Fig. 13).
6. The remaining half of the chamber was then filled with fused quartz particles in the same manner as 3 above.
7. The front panel was reinstated, and the chamber was rotated into its normal orientation. Finally, the top panel was removed in readiness for testing.

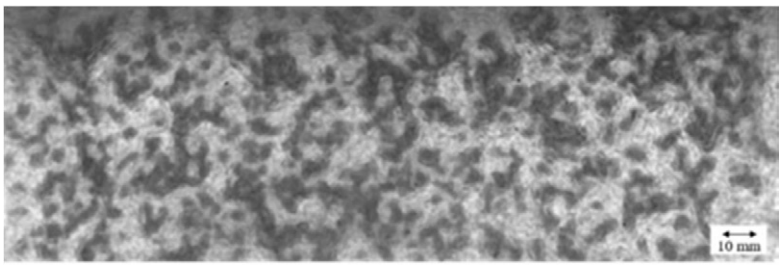

Figure 13: Example of speckled pattern viewed behind 140 mm thickness of transparent soil. (After Chen et al. 2022.)

A high-speed, 2.3-megapixel, monochrome camera was setup in front of the chamber to capture the movement of the black particles. Images were captured at 120 frames per second and at a resolution of 1920 × 1200 pixels, and subsequently analysed using the free MATLAB module GeoPIV_RG (Stanier et al. 2015) to quantify particle displacements. An example of the resulting displacement vectors is shown in Figure 14. The particle trajectories at regions A and B, for example, associated with the first pass are shown in Figure 15. As can be observed, the PIV analysis provides a unique and interesting insight into the particle displacements as a consequence of RDC. It is important to note, however, that by its nature, the transparent soil is fully saturated, which is atypical of field applications of RDC.

In order to measure surface displacements due to RDC, Chen et al. (2022) utilised an EinScan Pro+3D scanner (Shining 3D 2019), as shown previously in Figure 10c, to measure the average settlement of the ground surface. A characteristic of RDC is that it produces a non-uniform, undulating ground surface profile, and a 3D scanner provides an accurate and

effective means of sampling the ground surface. The manufacturers state that the EinScan Pro+3D scanner employs a non-laser, white light as the light source to generate a highly accurate (±0.05 to 0.3 mm) point cloud in a very efficient manner (550,000 points per second) (Shining 3D 2019). An example of a point cloud obtained from the surface of the transparent soil is shown in Figure 16.

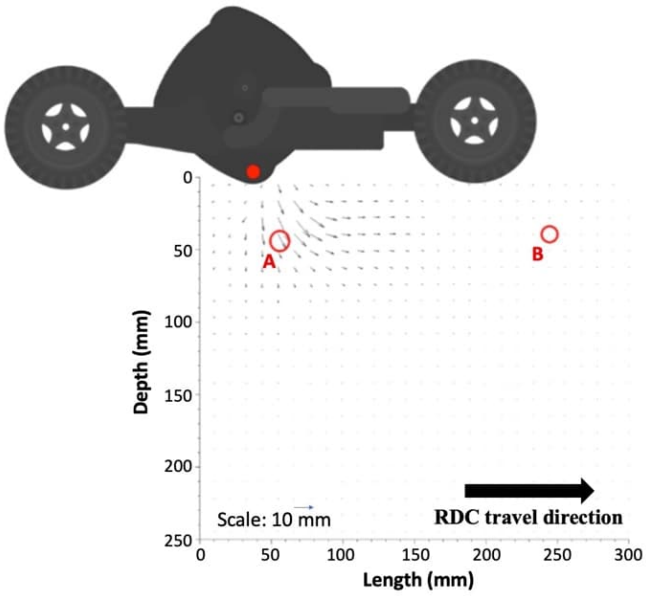

Figure 14: Example of displacement vectors for first pass of the 3.64 kg (BH-1300) roller at t = 0.23 s. (Adapted from Chen et al. 2022.)

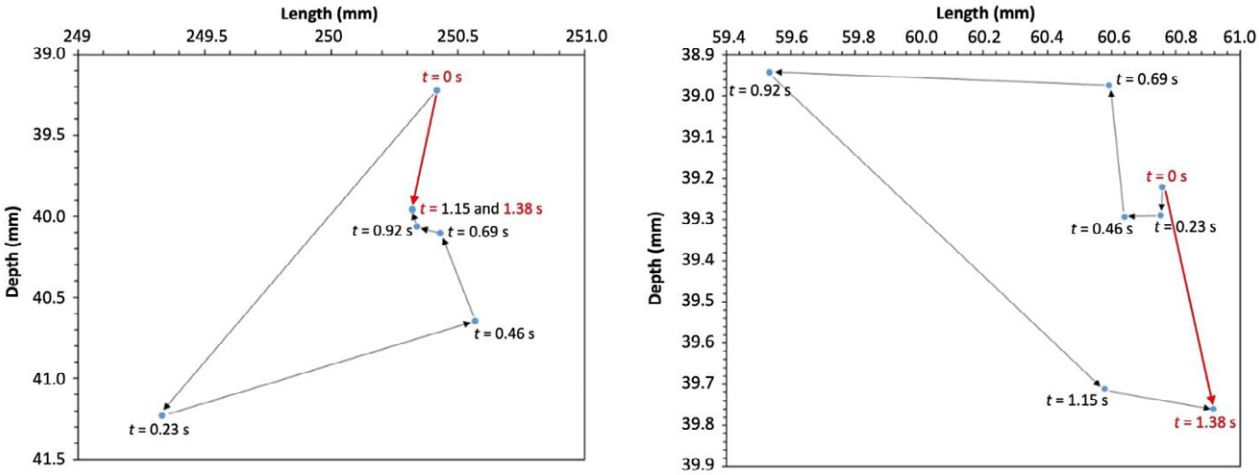

Figure 15: Particle trajectories associated with the first pass of the 3.64 kg (BH-1300) roller at regions: (a) A, and (b) B, as identified in Fig. 14. (Adapted from Chen et al. 2022.)

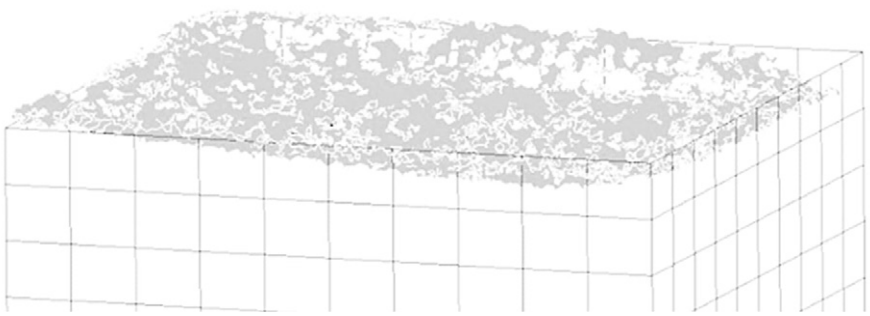

Figure 16: Example of point cloud from 3D scanner. (Adapted from Chen et al. 2022.)

From the point clouds, average surface settlements are obtained, as shown in Figure 17. Chen et al. (2022) performed scale model RDC testing at four different speeds: 214, 256, 299 and 342 mm/s. Accounting for the 1:13 model scale and applying the scaling laws developed by Altaee & Fellenius (1994), these speeds translate to prototype speeds of 10, 12 14 and 16 km/h, respectively, and the field surface settlements of 10 and 20 mm translate to 130 and 260 mm, respectively.

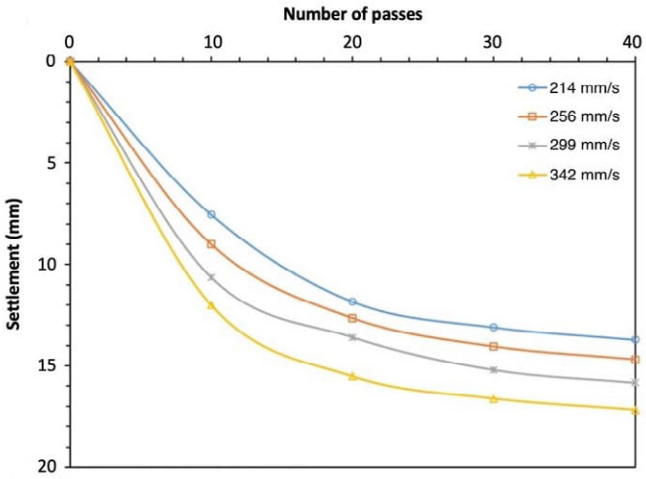

Figure 17: Average ground settlements associated with the 3.64 kg (BH-1300) roller at different speeds. (Adapted from Chen et al. 2022.)

The scale model testing performed on transparent soil by Chen et al. (2022) yielded the improvement depths indicated in Table 2. Other work performed by Chen et al. (2021a, b) has successfully correlated these experimental results with discrete element modelling and with field results obtained by Scott et al. (2019, 2021), and Chen et al. (2023a, b) has extended this work further, to incorporate other RDC configurations and soils.

Table 2: Improvement depths for the two scale models operating at different speeds. (Adapted from Chen et al. 2022.)

Scale model weight (kg) [Prototype model]	Operating speed (mm/s) [Prototype speed, km/h]	Improvement depth (mm) [Prototype depth, m]
3.64 [BH-1300]	214 [10]	130 [1.69]
	256 [12]	165 [2.15]
	299 [14]	230 [2.99]
	342 [16]	230 [2.99]
5.46 [BH-1300HD]	214 [10]	210 [2.73]
	256 [12]	220 [2.86]
	299 [14]	240 [3.12]
	342 [16]	230 [2.99]

3.3 MACHINE LEARNING

In relation to RDC, the final topic that I'd like to explore involves machine learning (ML), which is a subset of artificial intelligence (AI). In recent times, AI has become more ubiquitous and, its reach is growing exponentially. One of the great advantages of ML is that it is able to distinguish patterns, and therefore make predictions from the data alone, which is helpful when the relationships between the data lack clarity. Here, we'll explore the relationship between RDC and cone penetration tests (CPTs) using the ML technique of artificial neural networks (ANNs).

As we've seen from the preceding treatment, RDC improves the density of the ground with each pass of the module. There exists, however, for each site, an optimal number of passes, beyond which further improvement is modest. As one knows, measuring in situ density below the ground, particularly below depths of 0.5 m is difficult. Above 0.5 m, the nuclear density meter and/or sand replacement tests are generally adopted. Below 0.5 m, indirect tests, such as the CPT, dynamic cone penetration test and geophysical tests are generally used. However, because these tests do not directly measure density, correlations are required. The relationship between CPT measurements, for example, and density lacks clarity and

is complex. The question we'll ask ourselves then is: "Can one use CPT data from previous projects and sites to predict the level of improvement one might anticipate with additional RDC passes?"

Broons has been operating the 4-sided impact roller since 1984, and since that time, has completed many ground improvement projects over a wide range of soil types and ground conditions. Hence, many data are available to be interrogated. Another of my former PhD students, Dr. Tharanga Ranasinghe, compiled an extensive database of RDC measurements in order to develop ML models to predict RDC ground improvement (Ranasinghe et al. 2017a, b, 2019a, b).

In the interests of optimising space, a detailed treatment of the development of ANN models will not be given here. Instead, interested readers are directed to the Ranasinghe et al. (2017a, 2019a). Briefly, ANN models are usually developed by incrementally adjusting their architecture and internal parameters until optimal predictions are obtained. In the case of RDC and CPT measurements, an ANN model was developed adopting four input variables and one output variable, as shown in Figure 18. The inputs consisted of: (1) depth below ground, D (m); (2) initial cone tip resistance, q_{ci} (MPa) at depth D; (3) initial sleeve friction, f_{si} (kPa) at depth D; and (4) the number of passes, P. The sole output variable is the final cone tip resistance, q_{cf} (MPa) at depth D after P passes. The aim of this model is to predict the improvement in the cone tip resistance (q_{cf}) due to an additional P passes of the RDC module. Figure 18 also shows the standard architecture incorporated in an ANN model, which consists of an *input layer*, in this case with 4 nodes or inputs; a *hidden layer*, with 4 hidden layer nodes; and an output layer, here with a single node. This architecture is associated with the optimal model.

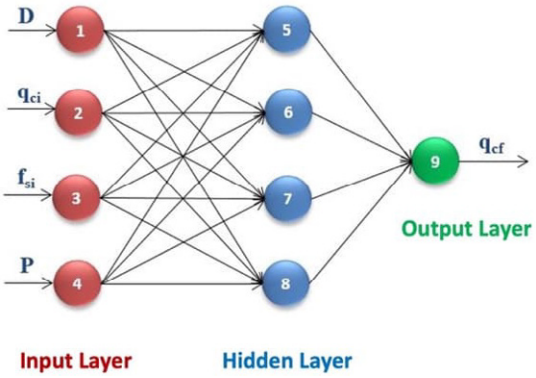

Figure 18: Optimal ANN model. (Adapted from Ranasinghe et al. 2019a.)

Machine learning techniques, like ANNs, are data-driven, and refine the connection weights between the nodes by being repeatedly exposed to data – both the inputs and the outputs. Prior to developing an ANN model, the data are typically subdivided into three data sets: training, testing and validation. The *training* set, which usually consists of the majority of the data, is used by the ANN to establish the connection weights. The *testing* set is used to minimise model overfitting, and the *validation* set is isolated from model, during the development phase, and used purely to test the veracity of the derived model. In the case of the RDC-CPT-ANN model, the entire dataset consisted of 1755 records from 91 CPTs, with 64%, 16% and 20% allocated to the training, testing and validation sets respectively.

A summary of the performance of the RDC-CPT-ANN model is shown in Figure 19, solely for the validation set. As can be seen, the model performs extremely well, recalling that these data were not exposed to the model during its development stage. In terms of statistical metrics, for the results shown in Figure 19, the correlation coefficient, R; mean absolute error, *MAE*; and root mean squared error, *RMSE*, are, 0.86, 2.93 MPa and 4.16 MPa respectively. Further details are provided by Ranasinghe et al. (2019a).

In a further effort to examine the performance of the ANN model, entire CPT soundings were predicted. CPTs were presented to the ANN model that were not part of the model development phase, as these data became available after the model had been created. Two such examples are presented in Figure 20. Whilst not perfect, one must conclude that the ANN performs admirably. Further examples are provided by Ranasinghe et al. (2019a).

One of the criticisms of artificial intelligence, and ANNs in particular, is their perceived lack of transparency. Critics will often state that ANNs are 'black boxes' and they provide little insight into the fundamental relationships between the input and output parameters. Whilst there is some merit in this sentiment, as mentioned earlier, ANNs have been shown to provide, on the whole, superior predictions to those obtained from traditional (i.e. non-AI) methods. The results shown in Figure 19 are but one example of this.

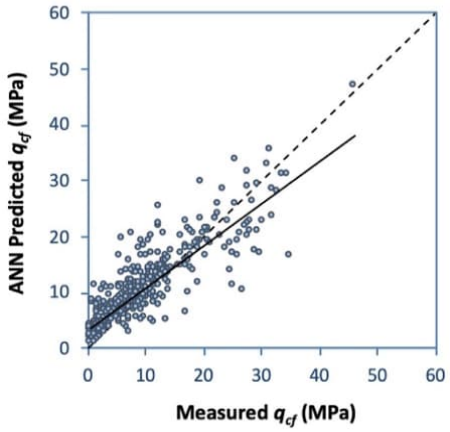

Figure 19: Validation set results from optimal RDC-CPT-ANN model. (Adapted from Ranasinghe et al. 2019a.)

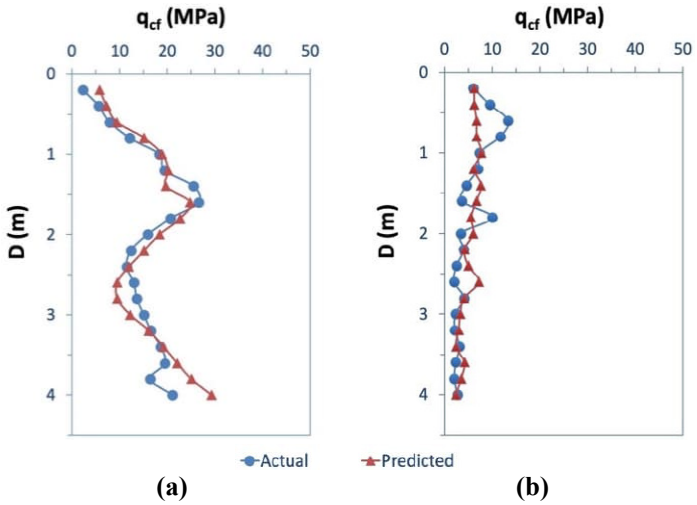

Figure 20: Plots of actual versus predicted CPT soundings from optimal RDC-CPT-ANN model: (a) Port Botany; (b) Potts Hill. (Adapted from Ranasinghe et al. 2019a.)

Another very important point to make here, is the flexibility that ANNs provide. Consider the problem at hand in this example; that is, quantifying the degree of ground improvement with depth as a result of increasing numbers of RDC passes in variable ground. Without doubt, the physical nature of RDC and ground improvement is extremely complex, and even measuring it in the field is non-trivial and indirect, as mentioned previously. Hence, one might ask oneself, if not for AI, how might one approach this problem? It is fair to say that the current state of numerical models, be they based on the finite element or discrete element methods, and their associated constitutive models, are simply not sophisticated enough to tackle such a problem.

The lack of transparency can also be rebutted, to a large extent, by the ability of ANNs to be translated to a relatively tractable equation; an example of which is given in Equation (3) for the RDC-CPT-ANN model. Admittedly, such an equation is generally only possible when the ANN model is parsimonious, such as that shown previously in Figure 18. Should the model have incorporated two or more hidden layers, a relationship, such as that shown in Equation (4), would not have been possible.

$$q_{cf} = \frac{62.738}{1 + \exp\left(T_5 + T_6 + T_7 - T_8 + 0.113\right)} - 6.104 \tag{4}$$

where:

$$T_5 = \frac{6.172}{1 + \exp\left(-0.251I_1 + 0.137I_2 - 0.002I_3 + 0.003I_4 + 1.889\right)}$$

$$T_6 = \frac{1.819}{1 + \exp\left(0.354I_1 + 0.025I_2 - 0.001I_3 + 0.03I_4 - 0.023\right)}$$

$$T_7 = \frac{0.916}{1 + \exp\left(0.15I_1 + 0.024I_2 - 0.0003I_3 + 0.008I_4 + 0.395\right)}$$

$$T_8 = \frac{3.82}{1 + \exp(-0.026I_1 - 0.057I_2 - 0.002I_3 + 0.052I_4 + 2.647)}$$

4 FUTURE: LUNAR GEOTECHNICS

Finally, in terms of the three research topics, I'd like to share some very recent work, which is a little 'out there' – literally! I was fortunate to grow up during the Apollo period; that is, during the United States of America's enormous undertaking to place humans on the Moon. As President John F. Kennedy so emphatically stated at Rice University on September 12, 1962:

> *"We choose to go to the Moon. We choose to go to the Moon in this decade and do the other things, not because they are easy, but because they are hard."*

You are likely aware that, after a hiatus of more than 50 years, the USA's National Aeronautics and Space Administration (NASA) has, through the Artemis program, established an ambitious goal to "send astronauts to the surface within four years, and build a long-term presence on the Moon by the end of the decade" (NASA 2020). It seeks to achieve its objectives in partnership with several private companies, including Boeing, Lockheed Martin, Northrup Grumman, Blue Origin, and SpaceX, as well as various space agencies, such as the European Space Agency (ESA) and the Japanese Aerospace Exploration Agency (JAXA).

The first Artemis mission (Artemis I) launched on November 16, 2022, was uncrewed and flew to the Moon to test the new Orion spacecraft, Space Launch System rocket and the ground systems at the Kennedy Space Center, Florida (NASA 2022a). The Orion spacecraft splashed down on December 11, 2022, and the mission was reported to have exceeded expectations (NASA 2023a). Artemis 2 will deliver a human crew into lunar orbit by 2024, and it is planned, with Artemis 3, to land humans on the Moon in 2025 (Space.com 2022).

Beyond NASA and the USA, there are many public and private organisations that also aspire to contribute to human habitation on other celestial bodies, such as the privately-owned Japanese company, ispace. On December 11, 2022, ispace launched their first mission (M1), which aimed to place its HAKUTO-R Mission 1 lunar lander on the Moon's surface. They state: "we believe that by 2040 the Moon will support a population of 1000, with 10,000 people visiting every year" (ispace 2023a). Unfortunately, on final approach on 26 April 2023, communication between the M1 lander and the ispace Mission Control Center was lost, and it was concluded that the lander most likely made a hard landing on the Moon's surface (ispace 2023b). Nevertheless, the mission marked a significant milestone for private investment in space exploration.

For a long-term presence on the Moon, infrastructure is essential, and civil and geotechnical engineers will play a critical and leading role in its design, construction and sustainability. At the University of Adelaide, as part of the Lunar Construction Group (LCG) within the Andy Thomas Centre for Space Resources (ATCSR), I and my colleagues have been exploring the geotechnical engineering aspects of lunar habitation and infrastructure development.

Before returning to lunar geotechnics, let's spend a moment considering the nature of the Moon and comparing it to the Earth. The Moon is, without doubt, an extremely hostile environment for humans. The Moon has virtually no atmosphere, and hence, is a near-vacuum. A single lunar day (i.e. the sidereal rotation time) is equivalent to 27.322 Earth days (Vaniman et al. 1991b). Hence, for approximately one-half of a month, the Moon is in darkness, and for the other half, it is in daylight. Because of this, the fluctuations in temperature on the Moon are large and extreme. The mean surface temperature on the Moon is 107°C during a lunar day and –153°C during the night, compared with 22°C on Earth (Vaniman et al. 1991b). At 1.62 m/s^2, the gravity on the Moon is one-sixth of that on Earth.

Other environmental factors on the Moon, which are perhaps less obvious but nonetheless important, are the ionizing radiation, i.e. solar and cosmic radiation, that the Moon is constantly subjected to; micrometeoroids that frequently bombard the lunar surface; the nuisance of electrostatically charged lunar dust that tends to adhere to any surface with which it comes into contact; and unusual lighting conditions (Vaniman et al. 1991b).

4.1 LUNAR TERRAIN AND ROCKS

The Moon's terrain has been influenced by two mechanisms, high-velocity impacts and volcanism (Vaniman et al. 1991b). As a result, there are two main terrain types: the heavily cratered and very old *highlands*, and the relatively smooth and younger *maria*. The mare basins are the Moon's dark regions, when observed from afar, and make up approximately 16% of the lunar surface, on the near side, and less than 1% of the Moon's far side (Vaniman et al. 1991a). They are surrounded

by high mountains that were formed during impact of planetesimals and many of these basins have been smoothed and filled or partly filled with basaltic lavas (Vaniman et al. 1991b). The highlands are generally lighter in colour than the maria, and they consist of a range of different rock types, including: ferroan *anorthosite* (which is believed to be from the Moon's original crust that formed between 4.6 and 4.3 billion years ago); *plagioclase-rich* rocks; *KREEP* rocks, which are highly enriched in potassium (K), rare earth elements (REE), and phosphorus (P); and *breccias* (Taylor et al. 1991).

NASA's Artemis Base Camp will be located at the lunar South Pole, essentially for two main reasons. Firstly, there are regions that are continuously exposed to sunlight, i.e. Mount Malapert (Harland 2016). This enables a continuous source of solar power. Secondly, there permanently shadowed regions, i.e. Shackleton Crater, where subsurface water ice has been discovered (NASA 2020). This is particularly helpful, as it can provide an available and ready source for potable water and the ingredients for rocket fuel; namely, oxygen and hydrogen (Harland 2016). The South Pole is situated in the lunar highlands.

Unfortunately, little is known about the ground at the South Pole of the Moon, as there have been no missions that have landed rovers there. In fact, the only Apollo mission that explored the lunar highlands was Apollo 16, and hence there is much to discover.

4.2 LUNAR REGOLITH

The lunar soil, or regolith as it is known, has been formed by continuous meteoroid impact over more than 4 billion years and is characterised as a well-graded silty sand. The regolith is a complex mixture of five basic particle types: crystalline rock fragments, mineral fragments, breccias, agglutinates, and glasses (Carrier III et al. 1991). Just like on Earth, the relative proportion of each particle type varies spatially and is dependent on the mineralogy of the source rocks and the geologic processes that the rocks have been subjected to. Nearly all of the lunar surface is covered by several metres to tens of metres of loose regolith (Vaniman et al. 1991b). Of course, because of the lack of liquid water and an atmosphere, lunar regolith is not subjected to the kind and extent of weathering that the ground experiences on Earth.

Between 1969 and 1972, a total of six Apollo missions landed successfully on the Moon, with a total of twelve astronauts who have walked on its surface. From these missions, a total of 382 kg of lunar rocks and soil from the Moon's surface was returned to Earth (NASA 2022b).

Since then, the regolith has undergone an extensive suite of geotechnical testing in laboratories on Earth, and the results are presented in detail by Carrier III et al. (1991). A total of 225 g was also returned to Earth from three successful USSR-launched Luna missions between 1969 and 1976 (Harland 2016), and more recently, the China National Space Administration's (CNSA) Chang'e 5 mission returned 1.7 kg of lunar regolith (CNSA 2020).

Several of the Apollo missions also involved the astronauts performing a variety of in situ tests, including core sampling and excavation. In the early 1970s, the USSR successfully landed and deployed two remotely controlled rovers, Lunokhod 1 and 2. Together, they performed approximately 1000 cone-vane penetrometer tests to depths of 100 mm (Carrier III et al. 1991). As part of the Chang'e 3, 4 and 5 missions, between 2013 and 2020, the CNSA has also successfully deployed three landers and rovers to the far side of the Moon. The Chang'e 3 rover incorporated a soil probe and ground penetrating radar, and the Chang'e 5 mission rover included a drill that could sample to 2 m depth (Liu et al. 2022).

Carrier III et al. (1991) provides an excellent summary of the geotechnical characteristics of lunar regolith, and states that the primary factors that affect its behaviour are bulk density, relative density, and temperature. A very brief overview of the main geotechnical characteristics of lunar regolith follows.

- *Particle size distribution:* In general, and according to the Unified Soil Classification System, the soil is a well-graded (i.e. poorly sorted), silty sand to sandy silt; SW-SM to ML. The median particle size is 40 to 130 μm, with an average of 70 μm. Approximately 10% to 20% of the soil is finer than 20 μm, and a thin layer of dust adheres electrostatically to everything that comes into contact with the regolith, such as spacesuits, tools, equipment and lenses. This is a particular problem for future lunar habitation because mechanical bearings, joints and seals, for example, can foul, thus making machines and equipment potentially inoperable.
- *Specific gravity:* Varies between 2.3 to >3.2, with a recommended value of 3.1.
- *Bulk density:* The current best estimate for the average bulk density of the top 150 mm of lunar soil is 1.50 ± 0.05 g/cm^3, and of the top 600 mm is 1.66 ± 0.05 g/cm^3.
- *Relative density:* The in situ relative density of lunar soil has been found to be about 65% (medium to dense) in the top 150 mm, increasing to more than 90% (very dense) below a depth of 300 mm.
- *Compressibility:* The recommended values of compression index, C_c, for loose regolith is 0.3, and dense regolith is 0.05.
- *Shear strength:* Depending on the relative density, suggested values for cohesion are 0.1 to 1 kPa, and internal angle of friction are between 30° to 50°.

4.2.1 Lunar simulants

As one would expect, access to NASA's lunar regolith samples is extremely limited. In addition, whilst 382 kg of the Moon's ground has been returned to Earth, much of it is consists of rocks. This has necessitated the manufacture of regolith surrogates, which are known as simulants. These are made from rocks on Earth that are crushed and mixed so that the final product has mineralogies and particle-size characteristics that are as close as possible to actual lunar regolith.

Various simulants have been created over the last few decades. The ATCSR, as part of its EXTERRES (Extra-terrestrial Environmental Simulation) Laboratory, owns a suite of lunar and Martian simulants. Agarwal et al. (2023) provides a comparison of the geotechnical characteristics of highlands and mare simulants with the those of lunar regolith. The authors studied three lunar simulants, all of which are manufactured by and available from Exolith Lab (2023). The three simulants examined were two highlands surrogates (LHS-1 and MAB-1 [mixed anorthosite and basalt]) and a lunar mare simulant (LMS-1). LHS-1 and MAB-1 are essentially identical. LHS-1 contains, by weight, 74.4% anorthosite, 24.7% glass-rich basalt, 0.4% ilmenite, 0.3% pyroxene and 0.2% olivine, whereas MAB-1 contains no ilmenite, pyroxene or olivine (Exolith Lab 2023). It is important to note that none of the simulants currently include agglutinates or nanophase iron, nor do they exhibit electrostatic behaviour. The work of Agarwal et al. (2023) suggests that the geotechnical characteristics of LHS-1 and MAB-1 are effectively the same and both appear to be very good surrogates of highlands lunar regolith.

4.3 GROUND IMPROVEMENT ON THE MOON

Much of the development of infrastructure on the Moon is likely to be undertaken by fleets of autonomous rovers and robots, and much effort is currently being directed globally to develop such equipment, as well as the associated services to facilitate them, such as NASA's Lunar Gateway (NASA 2023b). Earthworks is a critical aspect of the development of infrastructure and an important component of this is, of course, compaction. A key question, however, is: "What is the most effective means by which to compact regolith on the Moon?" Given the extensive areas of the lunar ground that need to be compacted, RDC is certainly an option, as is compaction by means of vibratory drum rollers or similar. Dynamic compaction, in other words heavy tamping, is unlikely to be suitable, as this method will probably generate substantial dust above the ground surface, which is likely to persist for lengthy periods of time, thus contaminating the lunar environment, which is undesirable.

Transporting an 8-tonne, 4-sided impact roller to the lunar surface, is probably sub-optimal. The impact roller on Earth is a hollow steel shell which is infilled with concrete. A credible alternative for a lunar application would be to transport a hollow shell to the Moon and then fill it in situ with regolith. In addition, SpaceX's Starship, which is currently under development, is a gamechanger because, with a reusable rocket, it can transport up to 100-tonnes of payload to the lunar surface (SpaceX, 2023).

As a first effort to examine the question posed above, Scott et al. (2023) undertook a laboratory-based compaction trial to explore the efficacy of RDC in a lunar context. For the purposes of this study, the University of Adelaide–Broons RDC laboratory test rig was adopted, along with the 1:13 scale, 4-sided impact roller module, which were shown previously in Figures 8 and 9 respectively. As explained by Scott et al. (2023), the two soil bins were carefully filled with MAB-1 simulant at two different initial densities. Given that it is not possible to moisture-condition the ground on the Moon, compaction was undertaken on dry simulant. With this in mind, the authors wondered whether the RDC module would indeed rotate on the dry, loose simulant, or simply act as a dozer, ploughing the soil aside. As outlined by Scott et al. (2023), the RDC did in fact rotate, even on the loose simulant, and improved the ground, as is evident from Figures 21 and 22.

4.4 FUTURE WORK

From a geotechnical engineering perspective, there is much to uncover regarding the Moon. Geotechnical site investigations at the lunar South Pole are currently being planned, and equipment and sensors developed. Chambers that simulate the lunar vacuum and extreme temperature range are also being developed to facilitate testing lunar regolith in a more authentic lunar environment. The ATCSR's LCG is currently contributing to these research endeavours. Naturally, such work will take many years of effort by a large number of individuals around the world, and by many and varied research groups. An example of LHS-1 simulant being examined in one of the ATCSR's regolith thermal vacuum chambers (rTVACs) is shown in Figure 23.

Beyond the Moon, humanity's immediate attention is drawn to Mars. Recently, geotechnical engineers have begun to study the ground on Mars (Delage et al. 2022). It goes without saying, that this presents the potential for an enormous body of research, exploration and discovery. Since the beginning of geotechnical engineering, one can finally and honestly say that the future of 'dirt' is really exciting!

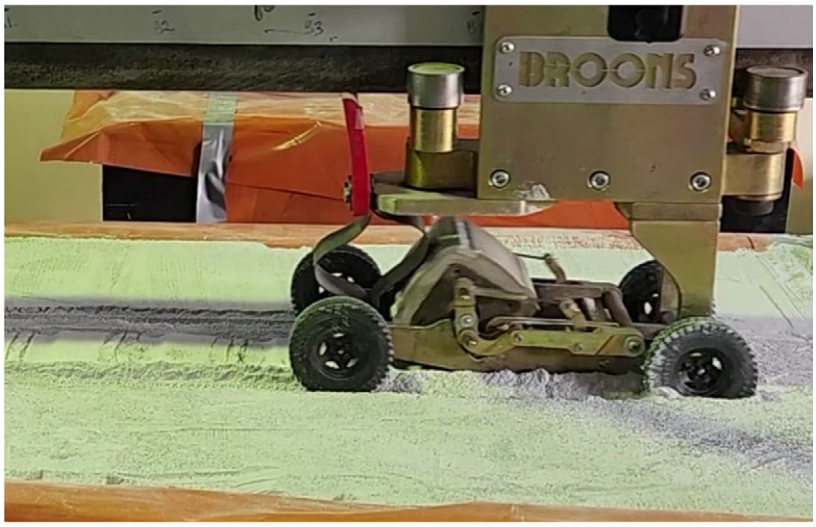

Figure 21: First pass of 1:13 RDC model on loose, dry MAB-1 simulant.

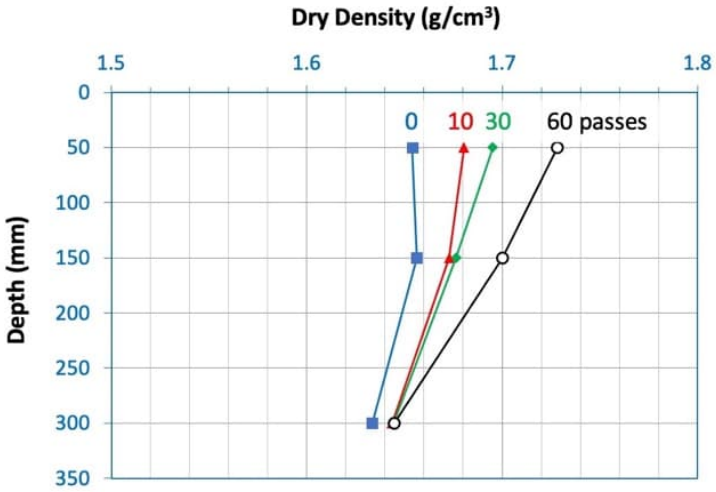

Figure 22: Dry density versus depth for varying numbers of passes. (Adapted from Scott et al. 2023.)

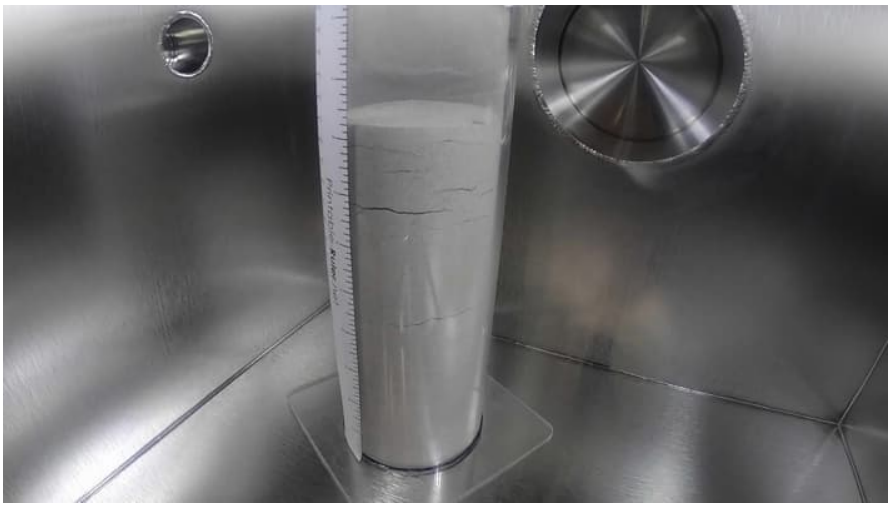

Figure 23: Loose LHS-1 simulant in an open-ended, polycarbonate tube during the process of applying a vacuum in one of the ATCSR's rTVACs. The horizontal cracks towards the top of the simulant core appear as the air in the regolith's voids off-gas, and they subsequently close up once the air has been vented.

5 DEMONSTRATION MODELS IN TEACHING

Finally, for those that know me and have attended my classes, will appreciate that teaching is one of my passions. In fact, for me, teaching is the main drawcard that attracted me into academia. In this final topic, I'd like to explore, albeit very briefly, the use of demonstration models in the teaching of geotechnical engineering, and how they can add great value; both in terms of enhancing understanding, and also engagement. Demonstration models are not new and have been used by many academics over the last several decades. Prof. John Burland from Imperial College in the UK, for example, has been a great advocate for their use (Burland 2008).

In the following sub-sections, I will discuss three models that my students and I have found helpful over the years, namely the: (i) consolidation model; (ii) vacuum-sealed coffee brick; and (iii) the liquefaction sand column. For the academics reading this, I hope that this might inspire and encourage you also to adopt demonstration models in your teaching. For those interested, this topic is explored in greater detail by Jaksa (2009).

5.1 CONSOLIDATION MODEL

A spring analogy, as shown in Figure 24, is often incorporated in many geotechnical engineering textbooks (e.g. Lambe & Whitman 1969, Holtz et al. 2011) to help explain the process of consolidation. I have found that, when converted to an actual physical model (Figure 25) and used in class, students are more readily able to understand the consolidation process, excess pore water pressure and its dissipation, and consolidation settlement.

In Figure 25, the stainless-steel spring (S) is an analogy of the soil skeleton; the water (W) in the transparent chamber represents the pore water; the gauge (G) measures the pore water pressure; the valve (V) represents the soil's permeability; and the steel weights (L) represent the applied load.

The demonstration proceeds in the following manner:

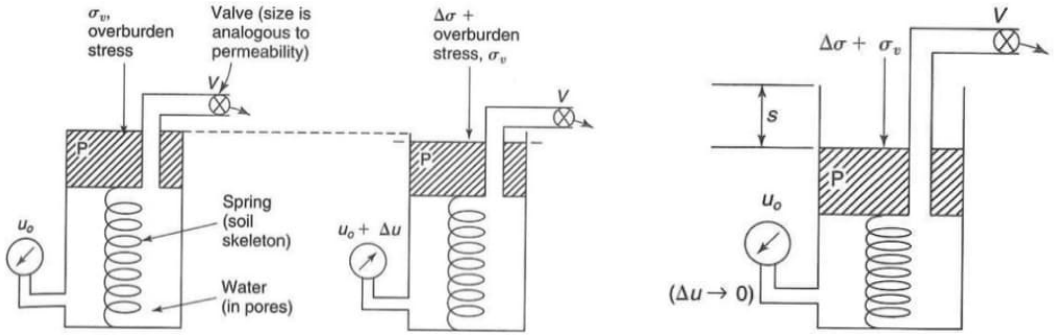

Figure 24. Consolidation spring analogy: (a) at equilibrium; (b) under load $\Delta\sigma$; and (c) under equilibriums at $\Delta\sigma + \sigma$. (After Holtz et al. 2011. Used with permission.)

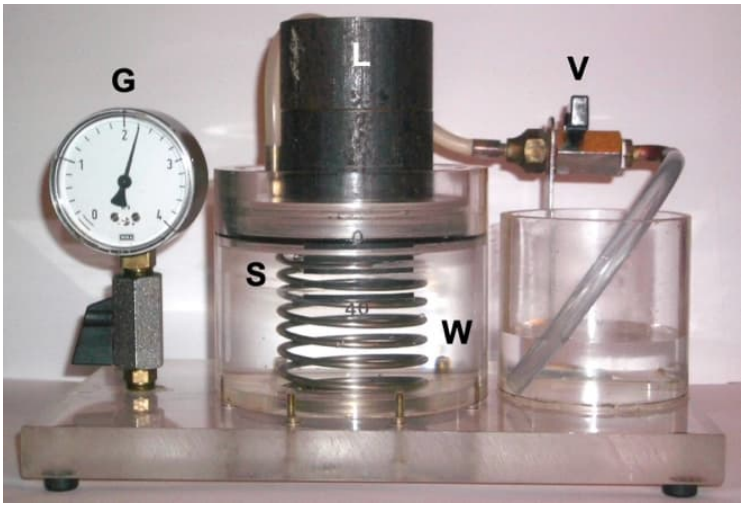

Figure 25: University of Adelaide consolidation model.

1. The valve is initially closed. This simulates the low permeability of fine-grained soils where drainage is extremely slow (Fig. 24a).
2. A series of loads is applied to the top platen of the consolidation model, and the pore water pressure rises with each load increment (Fig. 24b).
3. The valve is opened, and the water drains into the overflow beaker on the right, the pore water pressure decreases (i.e. dissipates), and the spring compresses – in other words, the soil settles (Fig. 24c).

A more detailed description of the demonstration, as well as specifications for the construction of the physical model, are provided by Jaksa (2009). In addition, a video of the demonstration itself is available on YouTube (Jaksa, 2020).

5.2 VACUUM-SEALED COFFEE BRICK

I have found, as have others (e.g. Atkinson 2007), that a readily available and very helpful physical model of the concept of effective stress is a vacuum-sealed brick of ground coffee, typical examples of which are shown in Figure 26.

At the beginning of my first lecture on effective stress, the two bricks of ground coffee shown in Figure 26 are handed around the classroom. It is mentioned that one has been punctured beforehand, thus compromising the vacuum seal, while the other's seal remains intact. The punctured brick is relatively soft and malleable, and the coffee grains can be easily moved around inside the packet, as shown by the brick on the left in Figure 26. In contrast, the other brick, whose vacuum-seal remains intact, is relatively hard and difficult to distort or indent with one's finger, as shown by the brick on the right in Figure 26. The students are encouraged to feel both bricks and suggest the reason for the difference in their behaviour, and then pass them on to the next student. Whilst the students are doing this, the lecture on effective stress proceeds.

Figure 26: Bricks of ground coffee (right: vacuum sealed; left: vacuum seal compromised). (After Jaksa 2009.)

At the end of the lecture the author asks whether anyone can suggest the reason for the difference between the two bricks. The answer is, of course, that the application of the vacuum has increased the inter-granular stress, i.e. the effective stress, which results in greater friction between the coffee grains, which increases the strength of the particulate mass. In this example, the pore fluid is air rather than water, and the pore air pressure is negative, due to the vacuum. The effective stress is therefore greater due to the negative pore (air) pressure.

A similar example to the vacuum-sealed coffee brick is that mentioned by Poulos (1994). It consists of a rubber glove filled with dry sand. When a vacuum is applied to the glove the strength of the sand increases, so much so that it is able to grasp a hammer.

A final example of the increase in strength of a particulate mass is that of a vacuum mattress, as shown in Figure 27. Such mattresses are used by emergency rescue personnel as a stretcher to immobilise patients and transport them over short distances, especially in cases of vertebra, pelvis, or limb trauma. The mattress is a sealed polymer bag that encloses small polystyrene balls, with a valve, straps and handles. In its flexible state, when the mattress valve is open and exposed to atmospheric pressure, the balls are relatively free to move, just like a bean bag, and the mattress can be moulded beneath and around the patient. Air is then withdrawn from the mattress through the valve by means of a hand-operated pump and the valve is then closed. The suction causes the balls to press together, and the mattress to become hard and rigid.

5.3 LIQUEFACTION SAND COLUMN

Lambe & Whitman (1969) introduced a conceptual model of a column of saturated sand to demonstrate the influence of pore water, excess pore water pressure and liquefaction. When the conceptual model is translated to a physical apparatus, as shown in Figure 28, it is a particularly useful teaching aid to facilitate a deeper understanding of pore water pressure, effective stress, the influence of flow direction on these, soil heave and liquefaction. Known as the liquefaction sand

column, this apparatus was developed at the University of Adelaide some time ago by my predecessors, as a laboratory-based device. More recently, I had the apparatus adapted, to make it portable by incorporating a small electric pump and a self-contained, recirculating water supply. In this way, the apparatus can be readily used as a demonstration aid in lectures. Student feedback has shown that it greatly enhances the understanding of the concepts mentioned above. Furthermore, it generates a great deal of engagement, both with the student body, but also with the general public and potential students, when it is used as a demonstration tool at expos and the like.

Figure 27: Vacuum mattress. (After Wikipedia 2023c.)

When demonstrating liquefaction, i.e. quicksand, an upward water flow in the sand column is established. The students are then asked to consider whether humans sink or float in quicksand. A brief excerpt is shown from a Tarzan movie (Tarzan and the Amazons) where Tarzan leads two villains into what appears to be a natural quicksand pit, upon which they are subsequently consumed by the quicksand, and they sink (supposedly) to the murky depths. A model human is then shown – another villain, this time from the 1960s marionette sci-fi series, the Thunderbirds (Wikipedia 2023b). It is explained that the figurine (shown standing at the bottom of Fig. 28) is a faithful reproduction of an actual human being, in that its specific gravity is close to unity. The students are again asked to decide whether the figurine will sink or float in the quicksand. The model is then lowered into the 'boiling' mix, and lo-and-behold, he floats! The students are asked to suggest reasons for why he floats.

Figure 28: Liquefaction sand column.

A downward flow of water is then established, followed by the creation of a v-shaped trench, using a spatula; a stable slope results. The valve permitting the vertical downward flow is then closed, thereby creating a no-flow situation. The v-shaped slope then collapses a little to a shallower slope angle. The valve which allows water to flow vertically upwards is then opened, immediately upon which the v-shaped slope totally collapses, so that the ground returns to being level. The students are then asked to explain this. The relationships between vertical flow, effective stress, soil strength and slope stability are then readily established.

Finally, liquefaction as a result of an earthquake is demonstrated. The water level in the sand column is lowered to just below the sand surface, thereby simulating the condition similar to that which occurred in Niigata, Japan prior to the 1964 earthquake. A solid brass model of a multi-storey building, weighing 5 kg, is then placed on the sand surface. The building settles a little when placed on the loose, saturated sand. A gentle tap on the side of the sand column causes the soil to liquefy and the building to topple, similar to the buildings in Niigata following the 1964 earthquake (Figure 29). The students are then asked to explain this.

An excerpt from the "Killer Quicksand" MythBusters episode (Wikipedia 2023a) is also shown, which involves the presenters creating a full-size liquefaction sand column. One of the presenters immerses himself in the device and demonstrates that humans do, in fact, float in quicksand.

A more detailed description of the demonstration, as well as specifications for the construction of the model, are provided by Jaksa (2009). In addition, three videos of the demonstration are available on YouTube (Jaksa 2023a–c).

Figure 29: Foundation failure due to liquefaction as the result of the 1964 Niigata earthquake. (After Uni. of Washington 2000.)

6 CONCLUSIONS

In this paper I have described but a small part of the varied nature of my journey in geotechnical engineering research and teaching over the last 35 years. My time has been both intellectually and personally rewarding, and I have enjoyed every minute; well almost! The following conclusions can be drawn from the material presented:

- Spatial variability of the ground can be modelled successfully using the mathematical technique of geostatistics. This method provides a useful, additional tool to derive predictions for preliminary analyses and to facilitate simulations.
- Kriging, coupled with a spherical model with a range of influence, a, of 1000 m; a nugget, C_0, of 1500 kPa^2; and a sill, $C + C_0$, of 2500 kPa^2 provides good preliminary predictions of the large-scale variability of the undrained shear strength of the Keswick Clay.
- Field studies have shown that rolling dynamic compaction (RDC), in the form of the 4-sided 'impact roller', is able to improve the ground to depths in excess of 3 m.
- Laboratory testing, using a 1:13 scale 1-g physical model incorporating transparent soil, provides useful insights into the effect of RDC on the ground and with depth. When coupled with discrete element modelling and the results from field trials, this work can be extended to other soils and RDC configurations.
- Machine learning, in the form of artificial neural networks (ANNs), facilitates the development of reliable models for the prediction of the extent of ground improvement due to RDC.

- Humankind's imminent foray into the Solar System provides exciting and practically limitless opportunities for fascinating geotechnical engineering research. Moreover, extra-terrestrial geotechnical engineering research has the potential to excite and engage school children and the public like almost nothing else.
- Three demonstration models have been presented, namely: the consolidation model; vacuum-sealed coffee brick; and the liquefaction sand column. Student surveys have shown that these demonstrations are very helpful in enhancing learning and student engagement.

7 ACKNOWLEDGEMENTS

There are numerous people that have assisted and nurtured me throughout my career. Of course, it goes without saying, that the love and support that I receive on a daily basis from my wife, children and my Creator, sustains me and I cannot thank them enough. Second, I thank my past and present students, for without their assistance, commitment and energy, the research would not have been done. I also extremely grateful to my geotechnical engineering colleagues, present and past – particularly Drs. Brendan Scott, Yien Lik Kuo, An Deng and William Kaggwa for their friendship and tremendous support over many years. The research involving rolling dynamic compaction would not have been possible but for the foresight and generosity of Stuart Bowes and Derek Avalle from Broons. I am grateful to them for facilitating this fascinating body of work. I also wish to thank the many academics from many institutions around Australia and the world, who have worked with me and who have been so kind. Finally, but not least, to my colleagues in the community that is the AGS, and especially the generous individuals who nominated me for this award; a huge thank you. I share this accolade with all of you.

8 REFERENCES

Agarwal, A., Kuo, Y.L., Jaksa, M.B. & Scott, B.T. 2023. Density, strength and compressibility characteristics of lunar regolith simulant. *Proc. of 14th Australia New Zealand Conf. on Geomechanics*, ANZ2023, Cairns.

Altaee, A. & Fellenius, B.H. 1994. Physical modeling in sand. *Canadian Geotechnical Journal*, 31, 420-431.

Atkinson, J. 2007. *The mechanics of soils and foundations*, 2nd ed., London: Taylor & Francis.

Burland, J.B. 2008. Personal reflections on the teaching of soil mechanics. *Proc. 1st Int. Conf. on Education and Training in Geo-Engineering Sciences: Soil Mechanics and Geotechnical Engineering, Engineering Geology, Rock Mechanics*, Constantza, Romania: 35-48.

Carrier III, W.D., Olhoeft, G.R. & Mendell, W. 1991. Physical properties of the lunar surface. In G.H. Heiken, D.T. Vaniman & B.M. French (eds), *Lunar sourcebook: A user's guide to the Moon*: Chap. 9: 475-594. Cambridge: Cambridge University Press.

Chen, Y., Jaksa, M.B., Kuo, Y.L. & Airey, D.W. 2021a. Investigating the effectiveness of rolling dynamic compaction (RDC) using discrete element method (DEM). *Granular Matter*, 23, 94.

Chen, Y., Jaksa, M.B., Kuo, Y.L. & Scott, B.T. 2021b. Discrete element modelling of the 4-sided impact roller. *Computers and Geotechnics*, 137.

Chen, Y., Jaksa, M.B., Kuo, Y.L. & Airey, D.W. 2022. Experimental analysis of rolling dynamic compaction using transparent soils and particle image velocimetry. *Canadian Geotechnical Journal*, 59 (2), 254-271.

Chen, Y., Jaksa, M.B., Kuo, Y.L. & Scott, B.T. 2023a. Numerical modelling of the 3-sided impact roller. *Computers and Geotechnics*, 157: Article 105331.

Chen, Y., Jaksa, M.B., Scott, B.T. & Kuo, Y.L. 2023b. A numerical parametric study of the effectiveness of the 4-sided impact roller. *Australian Geomechanics*, 58 (2): 45–59.

Chung, O.Y., Scott, B., Jaksa, M., Kuo, Y.L. Airey, D. 2017. Physical modelling of rolling dynamic compaction. *Proc. 19th Int. Conf. on Soil Mech. and Geotech. Engrg.*, Seoul, Korea: 905-908.

CNSA 2020. China's Chang'e-5 retrieves 1,731 grams of moon samples. China National Space Administration. Dec. 19. http://www.cnsa. gov.cn/english/n6465652/n6465653/c6810963/content.html (Accessed: 31/5/2023.)

Cox, J.B. 1970. A review of the geotechnical characteristics of the soils in the Adelaide city area. *Proc. Symp. on Soils and Earth Structures in Arid Climates*, Adelaide, Australia: 72-86.

Delage, P., Marteau, E., Golombek, M.P., Hurst, K., Banerdt, W.B., et al. 2022. The mechanical properties of the Martian soil at the InSight landing site. In M. Rahman & M.B. Jaksa (eds), *Proc. 20th Int. Conf. on Soil Mech. and Geotech. Engrg.*, Sydney, Australia, Vol. 1. State of the Art and Invited Lectures: 567-581.

Englund, E. & Sparks, A. 1991. *GEO-EAS 1.2.1: User's guide*. Las Vegas: Environmental Monitoring Systems Lab., U.S. Environmental Protection Agency. https://nepis.epa.gov/Exe/ ZyPURL.cgi?Dockey=940067XZ.txt (Accessed: 31/5/2023.)

Exolith Lab 2023. https://exolithsimulants.com (Accessed: 31/5/2023.)

Harland, D.M. 2016. *Moon: From 4.5 billion years ago to the present – Owners' workshop manual.* Sparkford: Haynes Publishing.

Holtz, R.D., Kovacs, W.D. & Sheahan, T.C. 2011. *An introduction to geotechnical engineering*, 2nd ed., Upper Saddle River: Pearson.

ispace 2023a. https://ispace-inc.com (Accessed: 31/5/2023.)

ispace 2023b. Status update on ispace HAKUTO-R Mission 1 Lunar Lander. https://ispace-inc.com/news-en/?p=4655 (Accessed: 31/5/2023.)

Jaksa, M.B. 1995. *The influence of spatial variability on the geotechnical design properties of a stiff, overconsolidated clay*, Ph.D. Thesis, Faculty of Engineering, The University of Adelaide.

Jaksa, M.B. 2006. Modeling the natural variability of over-consolidated clay in Adelaide, South Australia. In T.S. Tan, K.K. Phoon, D.W. Hight, S. Leroueil (eds), *Characterisation and engineering properties of natural soils*: 4, 2721-2751. London: Taylor and Francis.

Jaksa, M.B. 2009. Use of demonstration models in undergraduate geotechnical engineering education. *Research Report No. R177*, School of Civil, Env. & Mining Engrg., Uni. of Adelaide. https://www.researchgate.net/publication/274387253_Use_of_Demonstration_Models_in_Undergraduate_Geotechnical_Engineering_Education

Jaksa, M.B. 2020. Consolidation process – Physical model. YouTube: https://youtu.be/c3yY79L1JHc (Accessed: 31/5/2023.)

Jaksa, M.B. 2023a. Liquefaction: 1. The Hood. YouTube: https://youtu. be/Ja-JE7W35V0 (Accessed: 31/5/2023.)

Jaksa, M.B. 2023b. Liquefaction: 2. Slope stability. YouTube: https://youtu.be/kd3VlnoHYNc (Accessed: 31/5/2023.)

Jaksa, M.B. 2023c. Liquefaction: 3. Earthquake. YouTube: https://youtu. be/FBKFGIx9224 (Accessed: 31/5/2023.)

Jaksa, M.B., Airey, D.W., Scott, B.T., Kuo, Y.L., Ranasinghe, R.A.T.M., Bradley, A.C., Chung, O.Y., Li, Y. & Chen, Y. 2019. Quantifying the effect of rolling dynamic compaction. *Proc. 4th World Congress on Civil, Structural, and Environ. Engrg,*, Rome, Italy.

Jaksa, M.B., Kaggwa, W.S. & Brooker, P.I. 2000. Experimental evaluation of the scale of fluctuation of a stiff clay. In R.E. Melchers & M.G. Stewart (eds), *Proc. 8th Int. Conf. on the Application of Statistics and Probability*: 415-422. Rotterdam: Balkema.

Journel, A.G. & Huijbregts, Ch.J. 1978. *Mining geostatistics*. London: Academic Press.

Lambe, T.W. & Whitman, R.V. 1969. *Soil mechanics*. New York: John Wiley & Sons.

Li, Y., Airey, D.W. & Jaksa, M.B. 2022. Evaluating the effective depth of rolling dynamic compaction with a three-sided compactor. *Int. Journal of Physical Modelling in Geotechnics*, 22 (3), 128-142.

Liu, H., Xie, G. & Zhang, W. 2022. The first ever landing and experiments on the far side of Moon and future geotechnical considerations. In M. Rahman & M.B. Jaksa (eds), *Proc. 20th Int. Conf. on Soil Mech. and Geotech. Engrg.*, Sydney, Australia, Vol. 1. State of the Art and Invited Lectures: 561-566.

NASA 2020. *NASA's lunar exploration program overview*. National Aeronautics and Space Administration.

NASA 2022a. Artemis 1: We are going back to the Moon. National Aeronautics and Space Administration https://www.nasa.gov/ specials/artemis-i/ (Accessed: 31/5/2023.)

NASA 2022b. Lunar rocks and soils from Apollo missions. National Aeronautics and Space Administration https://curator.jsc.nasa.gov/ lunar/ (Accessed: 31/5/2023.)

NASA 2023a. Analysis confirms successful Artemis I Moon mission, reviews continue. National Aeronautics and Space Administration. Mar. 8. https://www.nasa.gov/feature/analysis-confirms-successful-artemis-i-moon-mission-reviews-continue (Accessed: 31/5/2023.)

NASA 2023b. Gateway. National Aeronautics and Space Administration. Feb. 1. https://www.nasa.gov/gateway (Accessed: 31/5/2023.)

Poulos, H.G. 1994. Patterns and practices in future geotechnical engineering education. *Proc. 13th Int. Conf. on Soil Mechanics and Foundation Engineering*, New Delhi, India: Vol. 5, 245-253.

Ranasinghe, R.A.T.M., Jaksa, M.B., Kuo, Y.L. & Pooya Nejad, F. 2017a. Application of artificial neural networks for predicting the impact of rolling dynamic compaction using dynamic cone penetrometer test results. *Journal of Rock Mechanics and Geotechnical Engineering*, 9(2), 340-349.

Ranasinghe, R.A.T.M., Jaksa, M.B., Pooya Nejad, F. & Kuo, Y.L. 2017b. Predicting the effectiveness of rolling dynamic compaction using genetic programming and cone penetration test data. *Proc. of Institution of Civil Engineers – Ground Improvement*, 170 (4), 193-207.

Ranasinghe, R.A.T.M., Jaksa, M.B., Kuo, Y.L. & Pooya Nejad, F. 2019a. Prediction of the effectiveness of rolling dynamic compaction using artificial neural networks and cone penetration test data, *Chinese Journal of Rock Mechanics and Engineering*, 38 (1), 153-170.

Ranasinghe, R.A.T.M., Jaksa, M.B., Kuo, Y.L. & Pooya Nejad, F. 2019b. Genetic programming for predictions of effectiveness of rolling dynamic compaction with dynamic cone penetrometer test results, *Journal of Rock Mechanics and Geotechnical Engineering*, 11 (4), 815-823.

Scott, B.T. & Jaksa, M.B. 2015. A field based study of the effectiveness of rolling dynamic compaction. In B. Indraratna, J. Chu & C. Rujikiatkamjorn (eds), *Ground improvement case histories: Compaction, grouting and geosynthetics*: Ch. 14, 429-452. Oxford: Butterworth-Heinemann.

Scott, B.T., Jaksa, M.B. & Mitchell, P.W. 2019. Ground response to rolling dynamic compaction. *Géotechnique Letters*, 9, 99-105.

Scott, B.T., Jaksa, M.B. & Mitchell, P.W. 2020. Influence of towing speed on the effectiveness of rolling dynamic compaction. *Journal of Rock Mechanics and Geotechnical Engineering*, 12 (1), 126-134.

Scott, B., Jaksa, M. & Mitchell, P. 2021. Depth of influence of rolling dynamic compaction. *Proc. of Institution of Civil Engineers–Ground Improvement*, 174 (2): 85-94.

Scott, B.T., Kuo, Y.L., Jaksa, M.B. & Agarwal, A. 2023. Compaction trial on lunar regolith. *Proc. 14th Australia New Zealand Conf. on Geomechanics*, ANZ2023, Cairns.

Shining 3D 2019. *EinScan-Pro series user manual*, version 3.0.0.0.

Space.com 2022. NASA's Artemis 3 mission: Landing humans on the moon. Nov. 16. https://www.space.com/artemis-3-moon-landing-mission (Accessed: 31/5/2023.)

SpaceX 2023. Starship. https://www.spacex.com/vehicles/starship (Accessed: 31/5/2023.)

Stanier, S.A., Blaber, J., Take, W.A. & White, D. 2015. Improved image-based deformation measurement for geotechnical applications. *Canadian Geotechnical Journal*, 53, 727-739.

Taylor, G.J., Warren, P., Ryder, G., Delano, J., Pieters, C. & Lofgren, G. 1991. Lunar rocks. In G.H. Heiken, D.T. Vaniman & B.M. French (eds), *Lunar sourcebook: A user's guide to the Moon*: Chap. 6: 183-284. Cambridge: Cambridge University Press.

University of Washington 2000. 1964 Niigata earthquake, Japan. Dept. Civil Engineering. https://depts.washington.edu/liquefy/html/ quakes/niigata/niigata.html (Accessed: 31/5/2023.)

Vaniman, D., Dietrich, J., Taylor, J. & Heiken, G. 1991a. Exploration, samples, and recent concepts of the Moon. In G.H. Heiken, D.T. Vaniman & B.M. French (eds), *Lunar sourcebook: A user's guide to the Moon*: Chap. 2: 5-26. Cambridge: Cambridge University Press.

Vaniman, D., Reedy, R., Heiken, G., Olhoeft, G. & Mendell, W. 1991b. The lunar environment. In G.H. Heiken, D.T. Vaniman & B.M. French (eds), *Lunar sourcebook: A user's guide to the Moon*: Chap. 3: 27-60. Cambridge: Cambridge University Press.

Wikipedia, 2023a. MythBusters. https://en.wikipedia.org/wiki/ MythBusters (Accessed: 31/5/2023.)

Wikipedia, 2023b. Thunderbirds (TV series). https://en.wikipedia.org/wiki/Thunderbirds_(TV_series) (Accessed: 31/5/2023.)

Wikipedia, 2023c. Vacuum mattress. https://en.wikipedia.org/wiki/Vacuum mattress (Accessed: 31/5/2023.)